Effects of post-subduction processes on continental lithosphere

Pilia S.[1], Davies D. R.[2], Hall R.[3], Bacon C.[1], Gilligan A.[4], Greenfield T.[1], Tongkul F.[5], Kramer S. C.[6], Wilson C. R.[7], Cornwell D. G.[4], Colli L.[8], Rawlinson N.[1]

[1] Department of Earth Sciences-Bullard Labs, University of Cambridge, Cambridge, UK.

[2] Research School of Earth Sciences, Australian National University, Canberra, AU

[3] SE Asia Research Group, Department of Earth Sciences, Royal Holloway University of London, Surrey, UK

[4] School of Geosciences, University of Aberdeen, Aberdeen, UK.

[5] Faculty of Science and Natural Resources, Universiti Malaysia Sabah, Kota Kinabalu, MY

[6] Department of Earth Science and Engineering, Imperial College London, London, UK.

[7] Earth and Planets Laboratory, Carnegie Institution for Science, Washington, DC, USA.

[8] Department of Earth and Atmospheric Sciences, University of Houston, Houston, USA.

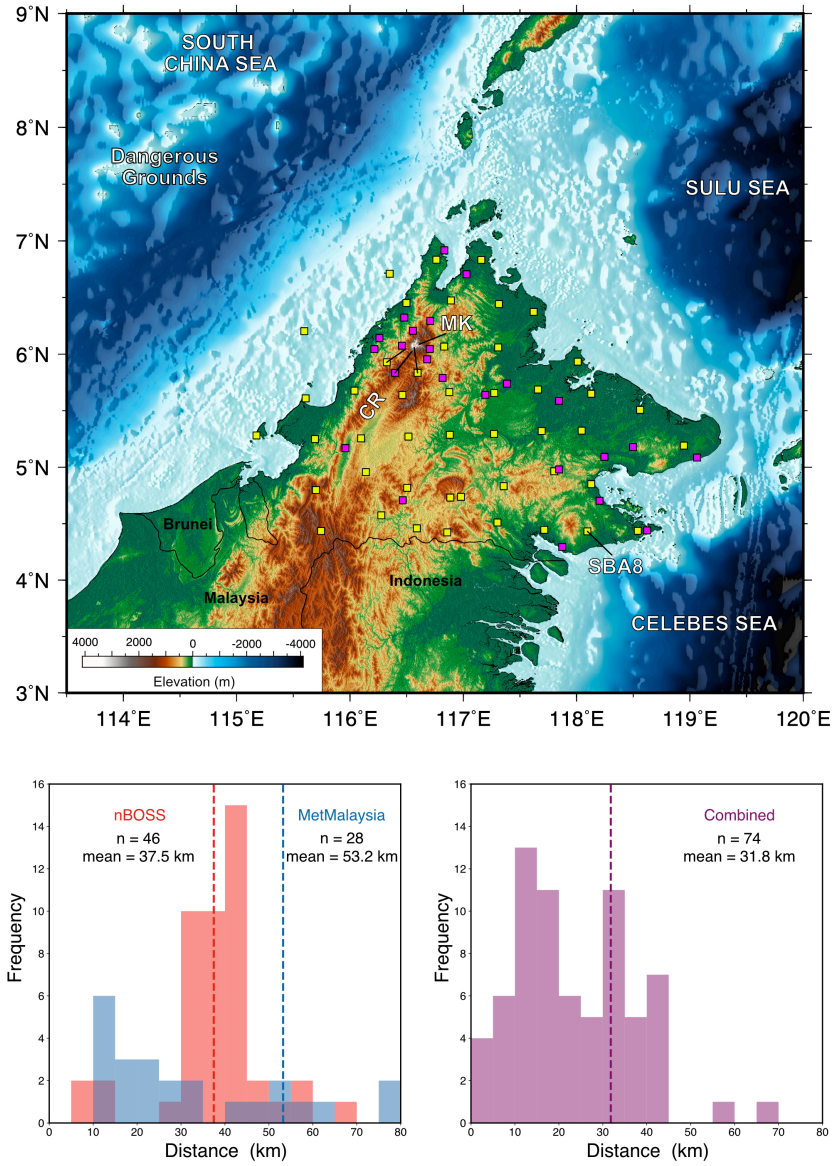

Extended Data Figure 1: nBOSS and MetMalaysia seismic networks. The nBOSS seismic experiment includes 46 temporary seismic stations (yellow squares), augmented by 28 permanent stations of the seismic monitoring network operated by the Meteorological Department of Malaysia (MetMalaysia, pink squares). Sensors of the nBOSS network deployed in the field are 3-component Güralp CMG-3ESPCDs (18 in total) and 6TDs (28 in total). MetMalaysia data are detected using Streckeisen STS-2 sensors. When the two seismic networks are jointly used (bottom histograms), they make a dense seismic network with an average station separation of 32 km, capable of resolving relatively fine structure below Sabah (for comparison, the USArray has an average station separation of ~70km). In this study we use all data available from the nBOSS network, which operated between March 2018 and January 2020. The same time window has been used for data generated by MetMalaysia. MK and CR denote the location of Mt Kinabalu and Crocker Range, respectively. Histograms in the lower panels illustrate the station separation of the nBOSS network with and without inclusion of MetMalaysia stations.

Crustal thickness estimates

Three-component seismograms for earthquakes of magnitude larger than 5, occurring between 30˚ and 90˚ epicentral distance from Sabah, were extracted from the continuous data records. A total of 85,518 seismograms were inspected and only those where the P arrival signal-to-noise ratio was high were taken forward for further analysis. After this initial quality control, a total of 14,447 seismograms were used to calculate radial receiver functions using the time-domain iterative deconvolution method[29] with a maximum frequency of approximately 1 Hz.

Receiver functions with a fit of less than 70% between the receiver function estimate convolved with the observed vertical component and the observed radial component were discarded. The remaining receiver functions were visually inspected and discarded if they appeared noisy, oscillatory, or anomalous compared to other receiver functions from a similar distance and backazimuth. This final quality control left a remaining dataset of 3,862 receiver functions. All the receiver functions at an individual station (Extended Data Figure 2 shows those for stations SBA8) were stacked together to reduce noise, yielding a stacked receiver function that is subsequently used in the joint inversion for shear-velocity structure.

1-D fundamental mode Rayleigh-wave group-velocity dispersion curves were extracted from the GDM52 global compilation[30] for each station location for a period range 25–250 s. At present this represents a reasonable group velocity data set for this region, including periods sensitive to both the crust and upper mantle. As the period range 25–250 s only constrains velocities in the lower crust and below, the surface wave data are primarily used here to ensure that the shear velocity values are realistic for this region to overcome the Vp/Vs-depth trade-off inherent in receiver-function data.

Dispersion curves and radial P receiver-function stacks for each station were inverted for shear velocity structure using *joint96*[31], an iterative non-linear least squares inversion method. Inversions are allowed to run until the misfit reduction is 0.005%, hence the number of iterations in the inversion is not the same for each station. Several different starting models have been tested including constant

values of 4.48 km/s, which is the uppermost mantle velocity in the ak135 model[47], 4.28 km/s, and 3.70 km/s, and Vp/Vs values of 1.79 down to 100 km, parameterized into 2 km thick layers, overlying ak135. Because none of these models preconditions crustal thickness, Moho structure recovered by the inversion is largely a function of the data. While there are some small variations between the solutions produced by the different starting models, they are sufficiently similar to not alter the interpretation of the structure.

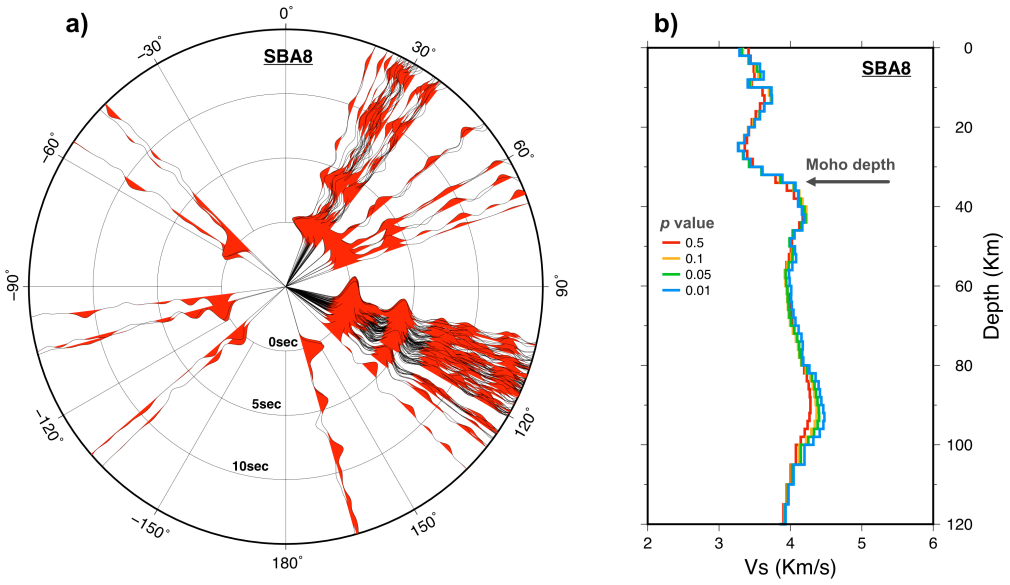

Extended Data Figure 2: Receiver function analysis: a) Receiver functions available for stations SBA8 (see Extended Data Figure 1 for location) shown in the backazimuthal range. Peaks at about 4 seconds indicate P-to-S conversions at the Moho. b) Moho depth and shear-wave velocity inversion using *joint96*.

In *joint96*, the relative weights for the receiver function and surface wave data are given by the *p* value, where the smaller the number, the greater the contribution from receiver functions. A *p* value of 0 means the inversion only includes receiver function data; a *p* value of 1 only includes surface wave data. We seek the model that has the maximum contribution from receiver functions but that maintains a good fit to the surface wave data, because the receiver functions have the greatest sensitivity to discontinuities such as the Moho. We tested *p* values of 0.5, 0.1, 0.05, and 0.01 (Extended Data Figure 2). Overall, the models show little variation in structure with *p* value, indicating that the resulting structures are robust.

68 The depth of the Moho beneath each station is picked from the 1-D shear velocity model, at the
69 depth that corresponds to the base of the steepest positive velocity gradient where shear velocity
70 exceeds 4 km/s.
71
72 **Shear-wave splitting analysis**
73 The presence of seismic anisotropy, the directional dependence of seismic wave-speed, has
74 been used to infer information about the dynamic state of the mantle for over 30 years. Under the right
75 conditions, the crystallographic axes of elastically anisotropic minerals (such as olivine and pyroxene)
76 will form a preferential alignment when deformed through dislocation creep. Through this process, the
77 microscopic anisotropy of the minerals is manifest on a macroscopic scale. When a linearly polarised
78 shear wave impinges on an anisotropic medium, it is partitioned into two quasi-S waves, which
79 propagate with different wave-speeds. The polarisation of these two waves, commonly called 'fast' (φ)
80 and 'slow', is determined by the symmetry and orientation of the anisotropic elastic tensor. A time lag
81 (*dt*) accrues between the waves while they propagate through the region, with the final integrated value
82 proportional to both the path length and strength of anisotropy.
83 A catalogue of viable earthquakes was produced containing only events with $M_b \geq 5.8$ and
84 epicentral distance ≥85˚, resulting in a total of 129 events. Arrival times for (S,SK,P,PK,SKI,PKI)KS
85 phases were predicted from a traveltime lookup table for each event/station pair. All waveform data
86 were bandpass filtered between 3 and 25 s before a signal-to-noise ratio was calculated in a window
87 around the theoretical arrival time. Only XKS arrivals with a signal-to-noise ratio exceeding 1.5 were
88 retained for splitting analysis. The waveform data were then inspected and the automatically assigned
89 analysis windows were re-picked, where necessary, to best capture the phase arrival. Poor quality,
90 noisy waveforms were also removed at this stage. The initial splitting analysis was performed using a
91 single channel transverse energy minimisation method[32], assuming a horizontal layer of anisotropic
92 medium. The resulting splitting measurements were then visually inspected and classified as 'good'

(clear and well-constrained splitting), 'fair' (clear evidence of splitting, but less well-constrained), 'null' (clear absence of splitting), and 'poor' (indeterminable result). Measurements classified as 'poor' were disregarded in further analysis.

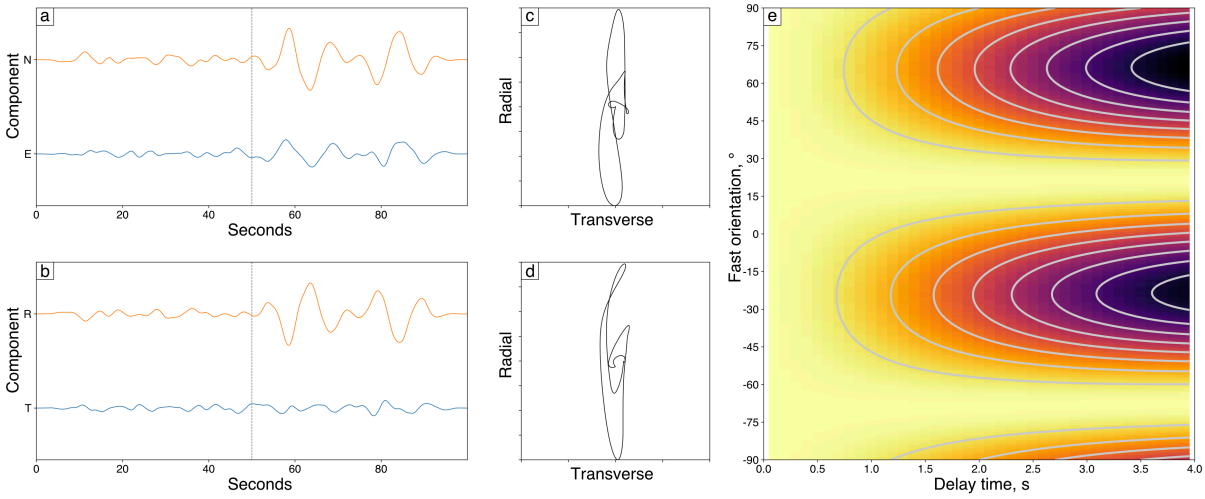

Extended Data Figure 3*:* Null measurement at SBA8. Panel a) shows the uncorrected north and east component data for an SKS arrival from a source located in the South Sandwich Islands. Panel b) shows the uncorrected data rotated onto the radial and transverse components. Panels c) and d) show the particle motions for the uncorrected and corrected waveform data, respectively. There is no evidence of elliptical particle motion in the uncorrected data, a key indicator of a null measurement. Panel e) shows the resultant energy grid from the splitting analysis, with the characteristic null pattern.

We present shear-wave splitting measurements at 62 stations across Sabah. 46 of these measurements stem from the nBOSS network, while the remaining 16 are from MetMalaysia instruments. Of these 16, one site (KKM, near Mt Kinabalu) has been in continuous operation since 2006, with data archived on the IRIS data centre. At this site there is little evidence of splitting parameters varying as a function of back-azimuth, though this does not preclude the possibility of second-order effects at other stations. The lack of shear-wave splitting measurements prevent us from investigating this further. Extended Data Figure 3 shows a good splitting measurement from station SBA8. Most of the null measurements at stations in central and western Sabah appear to be geometric (i.e., the back-azimuth is approximately aligned with the expected fabric). As such, the interpretation can be ambiguous. While anisotropy is likely to be present below these stations, we do not have good events at the right back-azimuths to validate this. Nulls detected in the Semporna Peninsula are not

well aligned with one of the nominal fast/slow axes, and hence are considered to be true nulls. For true nulls, one would expect to see null splits from any back-azimuth. Ultimately, as is typical with temporary seismic networks, we have not recorded a sufficient number of earthquakes to allow for a complete azimuthal coverage at most of the stations.

P-wave traveltime inversion

A total of 787 teleseismic sources were initially selected from the ISC catalogue; this includes all earthquakes from any depth with M_b larger than 5, and M_b larger than 4.6 if it occurred at a depth greater than 150 km.

A variety of P-wave phases, including direct P, pP, Pdiff, ScP, PcP and PKiKP are targeted and extracted from the continuous seismic dataset after the application of a bandpass filter with corner frequencies of 0.05 and 4 Hz. While most of the arrival times are typically from first-arriving P waves, the addition of core and reflected phases means that we can use seismic rays from outside the typical epicentral distance of 27˚-90˚, which can have different incidence angles. All extracted seismic traces have been initially aligned using the ak135 model[47] (Extended Data Figure 4) and stacked to produce an initial reference trace. Relative P-wave traveltime residuals have been subsequently extracted using an adaptive stacking technique[37], which uses the coherency of global phases across the entire network. Iterative improvement of the alignment by comparing the reference trace with each station trace is applied, which ultimately leads to an estimate of the residuals and associated picking error.

At this stage, all sources recorded by at least seven stations, and with an average uncertainty estimate of the residuals less than 0.12 seconds are retained (see Extended Data Figure 5 for two examples of arrival-time residual maps). After visually inspecting and selecting traveltimes on a source-by-source basis, 30671residual times are used to invert for 3-D velocity structure. This is achieved by using a grid-based eikonal solver and a subspace inversion technique implemented in FMTOMO[40].

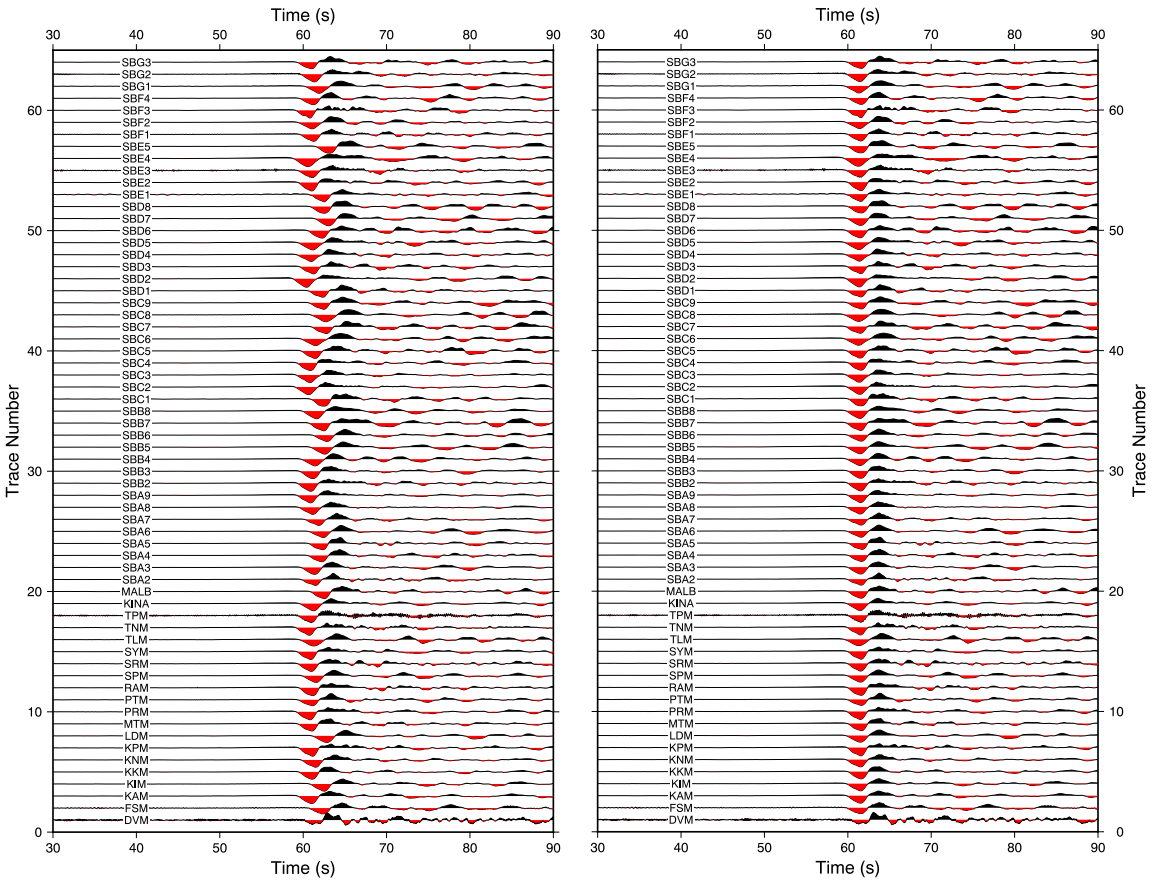

Extended Data Figure 4: Calculation of arrival-time residuals. Seismic records of an earthquake located in northern New Zealand. Left – Seismic traces aligned using the reference model ak135. Right – Trace move out corrected for using an adaptive stacking technique.

The non-linearity of the inverse problem is addressed by running six iterations of the subspace scheme, and updating the path and traveltime information using the multistage Fast Marching Method at the end of each iteration. The level of imposed regularisation is controlled by the damping and smoothing parameters, calibrated after examination of L-curves to provide the optimum tradeoff between data fit and model roughness. Our final tomographic model, shown through a series of horizontal slices in Extended Data Figure 6, yields a variance reduction of 87%.

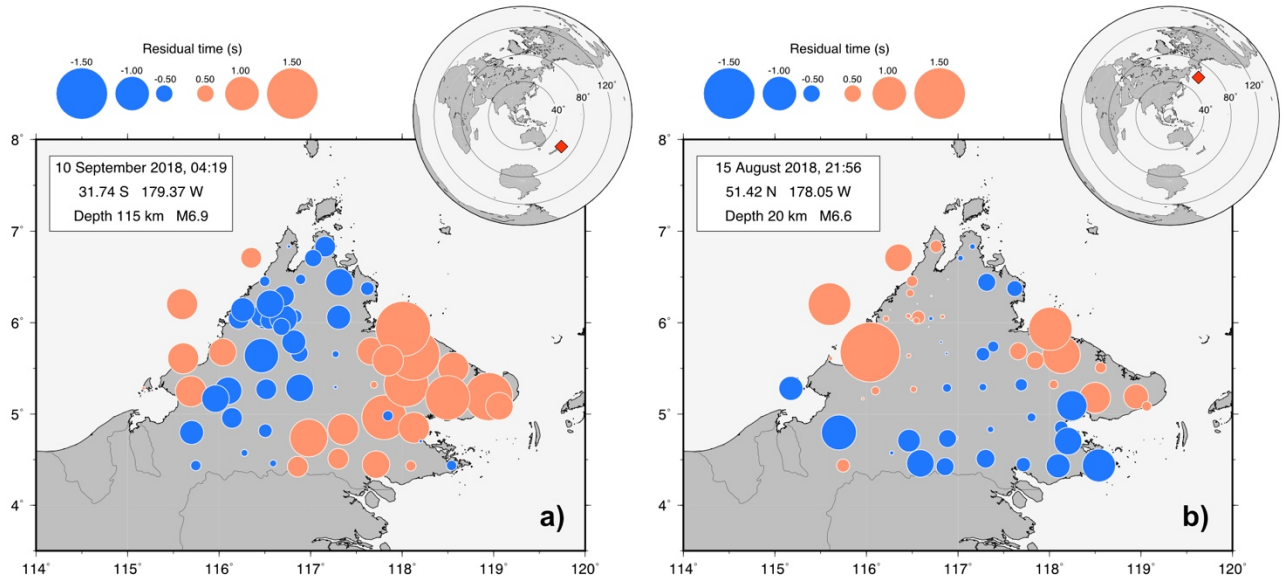

Extended Data Figure 5: Map of arrival-time residuals from two earthquakes. Relative arrival-time residual patterns (in seconds) from two different sources located in northern New Zealand (a) and Japan (b). Location of the seismic sources is illustrated in the upper right insets with red diamonds. Alignment of the seismic traces for residuals illustrated in a) are shown in Extended Data Figure 4. Note the dependence of the residuals pattern on the source backazimuth.

In order to confirm the dip and spatial extent of the high-velocity anomaly presented in Figure 2d (SD) of the main text, we have conducted two resolution tests based on synthetic data (Extended Data Figure 7). The synthetic data are created by applying the forward calculator (FMM), using the same source-receiver configuration as the observational dataset, in the presence of synthetic structure resembling a vertical and a tilted drip, and adding Gaussian noise with a standard deviation of 100 ms in order to simulate the noise content of real data, which includes picking uncertainty. As in the inversion of observed residual arrival-times, the 3-D volume is discretised into two layers (crust and mantle) with the spatial distribution of velocity nodes equal to 20 km in all directions, and every 10 km for the propagation grid (used by FMM in the forward step). Examples of the resolution tests are shown in Extended Data Figure 7, which indicate that both the vertical and lateral location of the synthetic high-velocity anomaly is resolved with a high degree of confidence. Additionally, our synthetic test demonstrates that we can recover with equal confidence the dip of the synthetic structure.

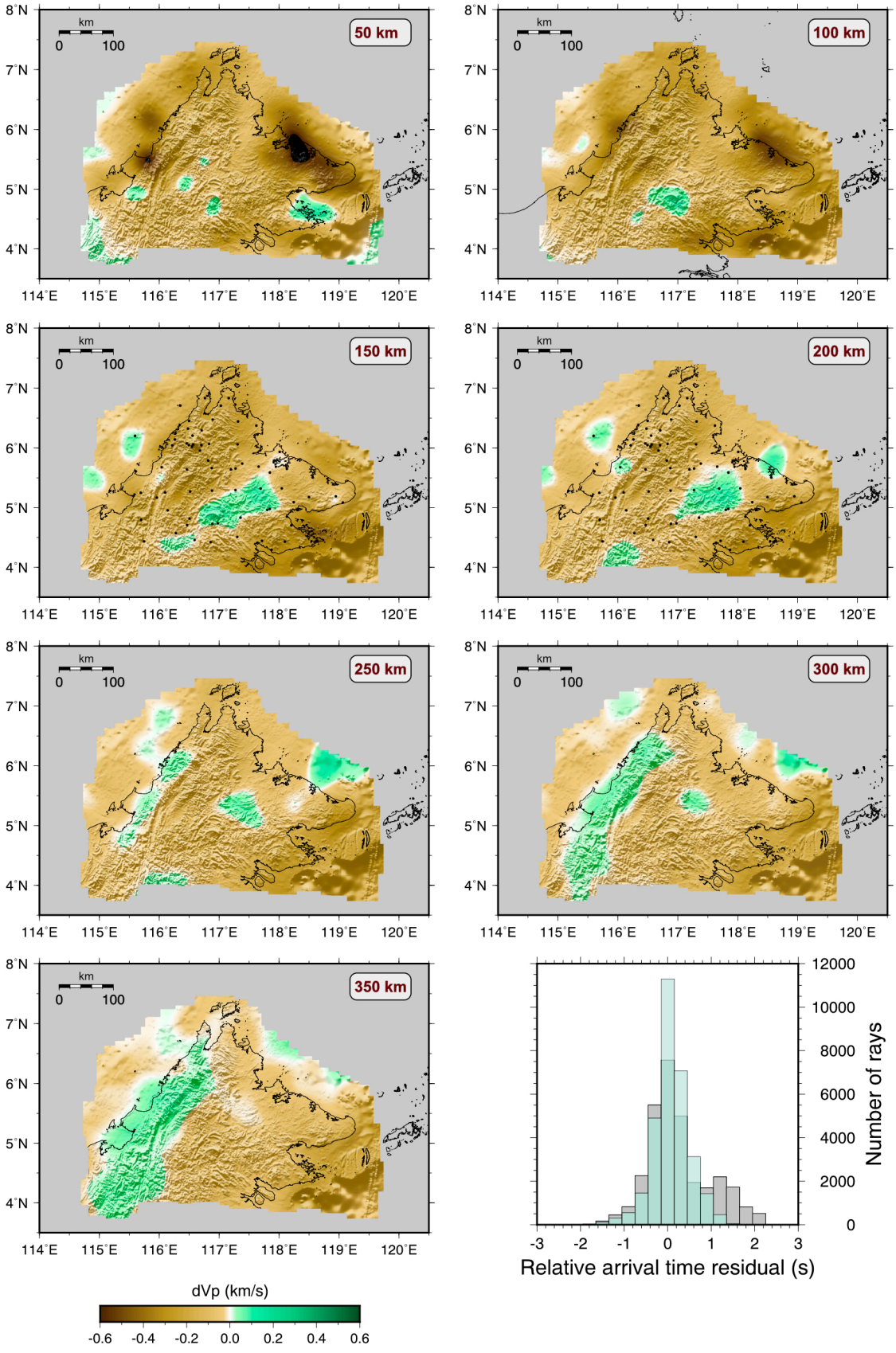

164

165 **Extended Data Figure 6: P-wave tomographic model.** Horizontal slices taken from the final P-wave
166 tomographic model every 50 km in depth. Black dots at depths of 150 and 200 km show the location of the

seismic sensors. Histogram shows the distribution of relative arrival-time residuals for the initial (grey) and solution (aqua green) model.

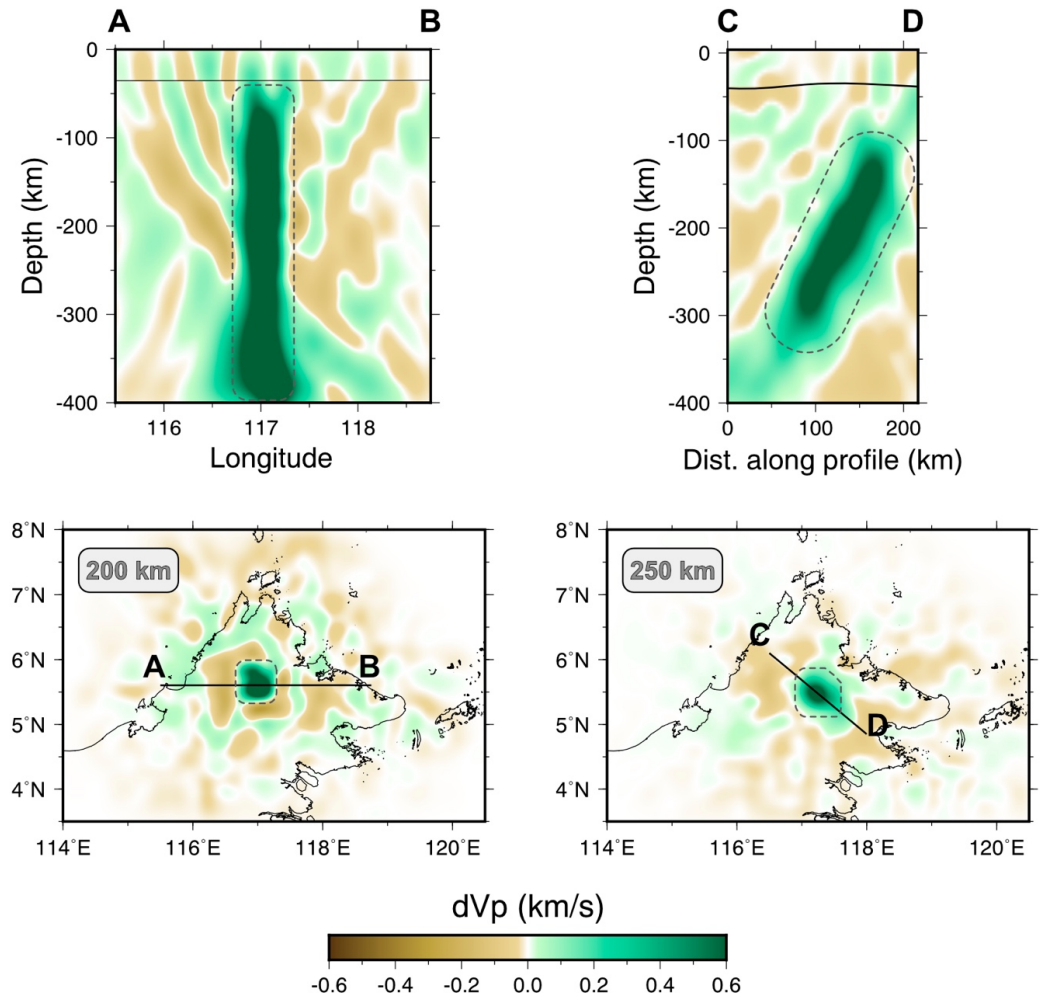

Extended Data Figure 7: Resolution tests. Resolution test based on synthetic structures involving a vertical (profile A to B) and tilted (profile C to D) high-velocity anomaly. Gray dashed line indicates the location of the input synthetic structure. Heterogeneity that lies outside the recovered target structure is largely a function of the random noise that is added to the data.

174 **Extended Data Table 1.** Physical parameters used in simulation.

175

Parameter	Upper crust	Lower crust	Mantle	Seed
Reference Density, ρ_0 (kg m^{-3})	2700	2850	3300	3340
Thermal expansion coefficient, α (K^{-1})	2.7 x 10^{-5}	2.7 x 10^{-5}	3 x 10^{-5}	3 x 10^{-5}
Gravity, g (m s^{-2})	9.8	9.8	9.8	9.8
Gas constant, R (J K^{-1} mol^{-1})	8.3145	8.3145	8.3145	8.3145
Thermal diffusivity, k (m^2 s^{-1})	1 x 10^{-6}	1 x 10^{-6}	1 x 10^{-6}	1 x 10^{-6}
Maximum viscosity, μ (Pa s)	1 x 10^{24}	1 x 10^{23}	1 x 10^{24}	1 x 10^{24}
Minimum viscosity, μ (Pa s)	1 x 10^{19}	1 x 10^{19}	1 x 10^{19}	1 x 10^{19}
Heat production, H (W m^{-3})	1.3 x 10^{-6}	2.7 x 10^{-7}	1.0 x 10^{-8}	1.0 x 10^{-7}
Diffusion creep rheology				
Activation energy, E (kJ mol^{-1})	-	-	300	300
Activation Volume, V (cm^3 mol^{-1})	-	-	4	4
Prefactor, A (Pa^{-1} s^{-1})	-	-	3 x 10^{-11}	3 x 10^{-11}
Dislocation creep rheology				
Activation energy, E (kJ mol^{-1})	-	-	540	540
Activation Volume, V (cm^3 mol^{-1})	-	-	12	12
Prefactor, A (Pa^{-n} s^{-1})	-	-	5 x 10^{-16}	5 x 10^{-16}
n	-	-	3.5	3.5
Peierls creep rheology				
Activation energy, E (kJ mol^{-1})	-	-	540	540
Activation Volume, V (cm^3 mol^{-1})	-	-	10	10
Prefactor, A (Pa^{-n} s^{-1})	-	-	10^{-150}	10^{-150}
n	-	-	20	20
Yield Strength Law				
Surface yield strength, τ_0 (MPa)	2	2	-	-
Friction coefficient, f_c (-)	0.2	0.2	-	-
Maximum yield strength, τy,max (MPa)	100	2	-	-

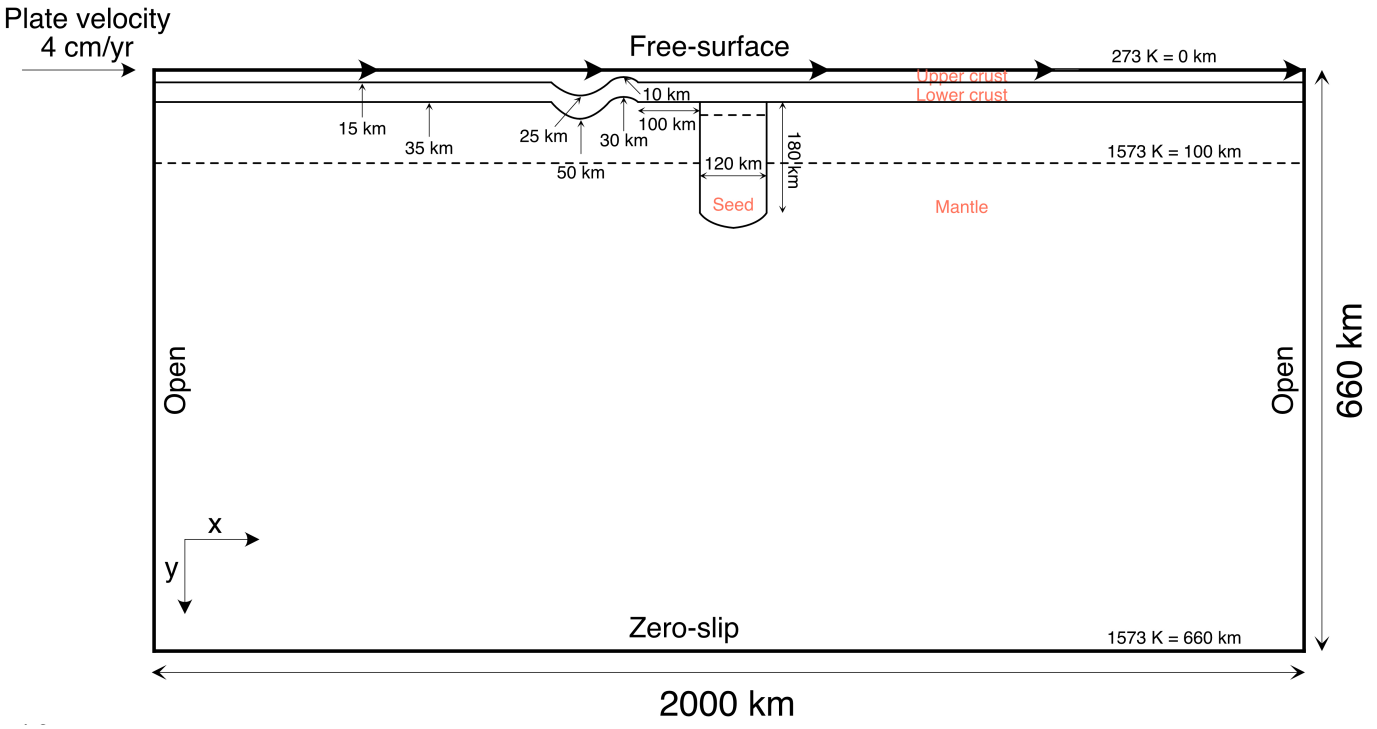

Extended Data Figure 8: 2-D numerical model setup and initial conditions. At the top boundary, x-velocities of 4 cm/yr are prescribed to mimic regional plate motion. The y-component is left free and is integrated in time to track free-surface elevation. The computational domain is adjusted continuously to match this elevation through a mesh movement procedure. A zero-slip boundary condition is imposed at the bottom of the model, with open, hydrostatic sides. Temperature boundary conditions are set to 273 K at the surface and 1573 K at the base, with insulating sidewalls. Our model includes 4 different materials (labelled in orange): upper-crust, lower-crust, a higher density seed and underlying mantle.

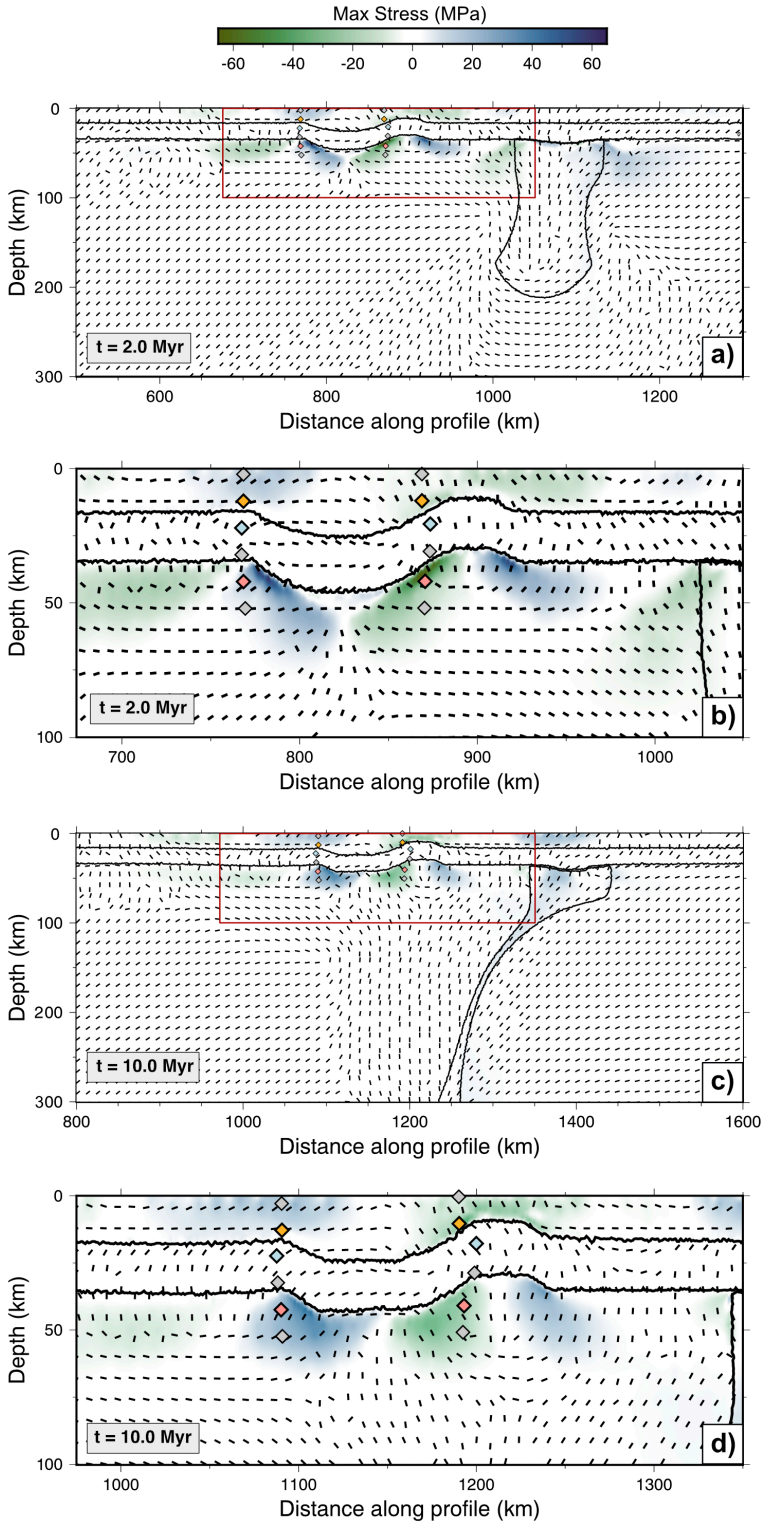

Extended Data Figure 9: Stress, tension and particles dynamics. Background maps illustrate distribution of stress magnitude in the horizontal direction at simulation times of 2.0 (a and b) and 10.0 Myr (c and d), respectively. Principal directions of tension are shown as black bars. Red rectangles in a) and c) show zoom-in areas on the region of thick crust for b) and d), respectively. Note how the principal directions of tension indicate the area of thick crust is under predominant extension. This is also illustrated by relative motion between corresponding pairs of Lagrangian particles, shown as coloured diamonds. Note how the stress magnitude has decreased by the end of the simulation at 10 Myr. Black lines represent the contours of the interfaces between different materials (upper crust, lower crust, dense seed and upper mantle).

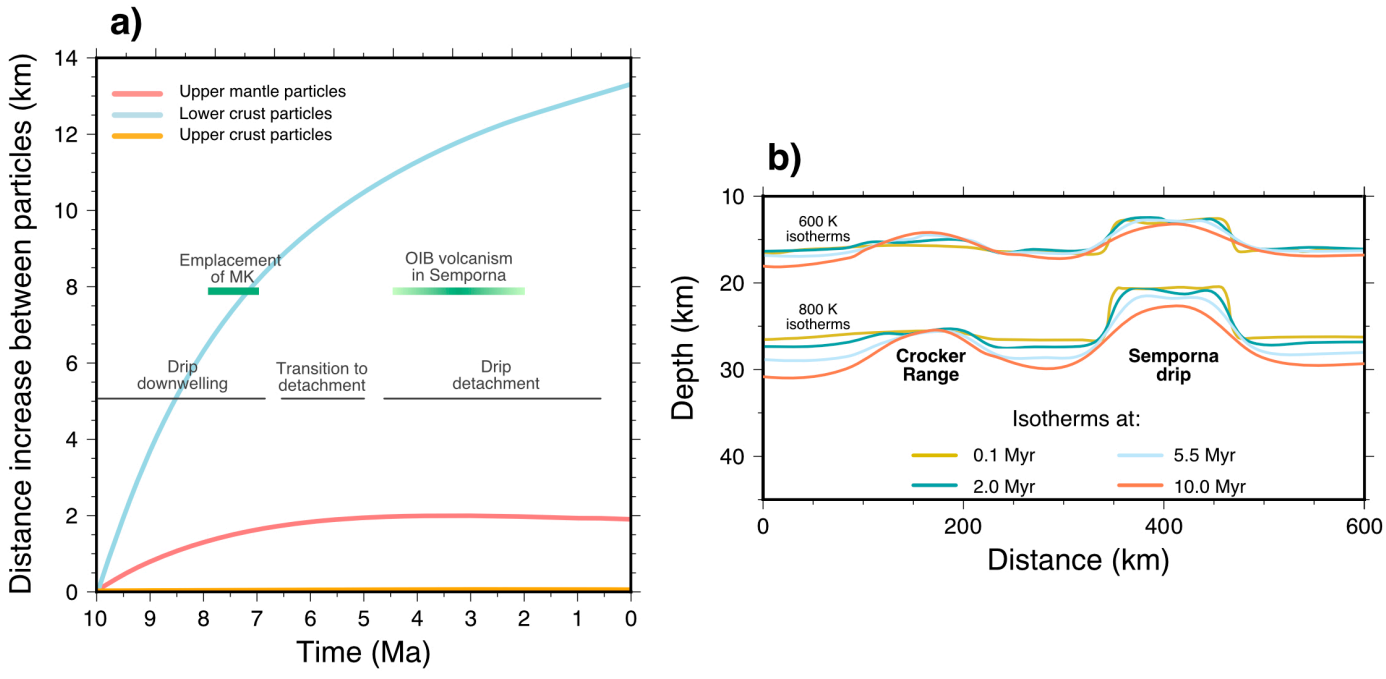

194 **Extended Data Figure 10: Upward deflection of isotherms and stretching in the Crocker Range.** a) The
195 increase in distance between two particles located in the upper crust (orange), lower crust (light blue) and upper
196 mantle (light red) throughout the simulation. Zero distance corresponds to the onset of simulation, where all
197 particles are 100 km apart. Time is expressed in Ma (million years before present) to match age of main tectonics
198 events (10 Ma equals onset of simulation). Particle locations are also shown in Extended Data Figure 9 with
199 consistent colours. Increasing distance between particles is a proxy for extension in the Crocker Range, which
200 is intimately tied to the drip, as it descends away from the surface into the underlying mantle. b) Evolution of
201 600 and 800 K isotherms at different stages of the simulation. Extension in the lower crust of the Crocker Range
202 is accompanied by an upward deflection of these isotherms relative to adjacent areas. To allow for
203 straightforward comparison, isotherms from different simulation times have been aligned under the area of thick
204 crust, coincident with the Crocker Range.

205

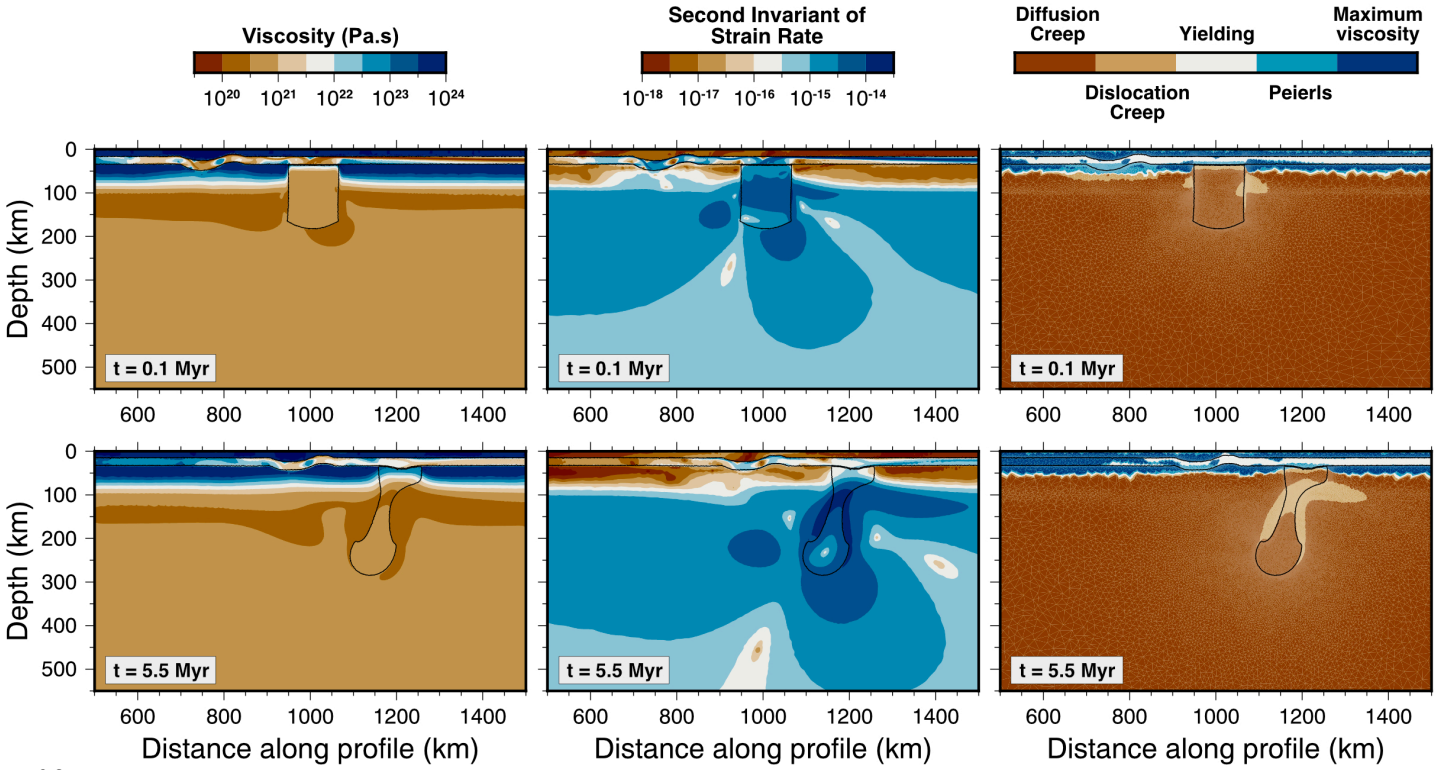

Extended Data Figure 11: Snapshots of viscosity, the second invariant of strain-rate and the dominant deformation mechanism. Time in Myr from start of simulation. Black lines delineate the interface between different materials (upper crust, lower crust, dense seed and upper mantle). Note how the area of thick crust exhibits high strain-rates, evident at t=0.1 Myr, which localises yielding and deformation. As the simulation evolves and the drip descends into the underlying mantle, this region remains weak, which facilitates lower-crustal extension. In the underlying mantle, material deforms principally through diffusion creep, aside from regions very close to the drip, where higher strain-rates promote dislocation creep.

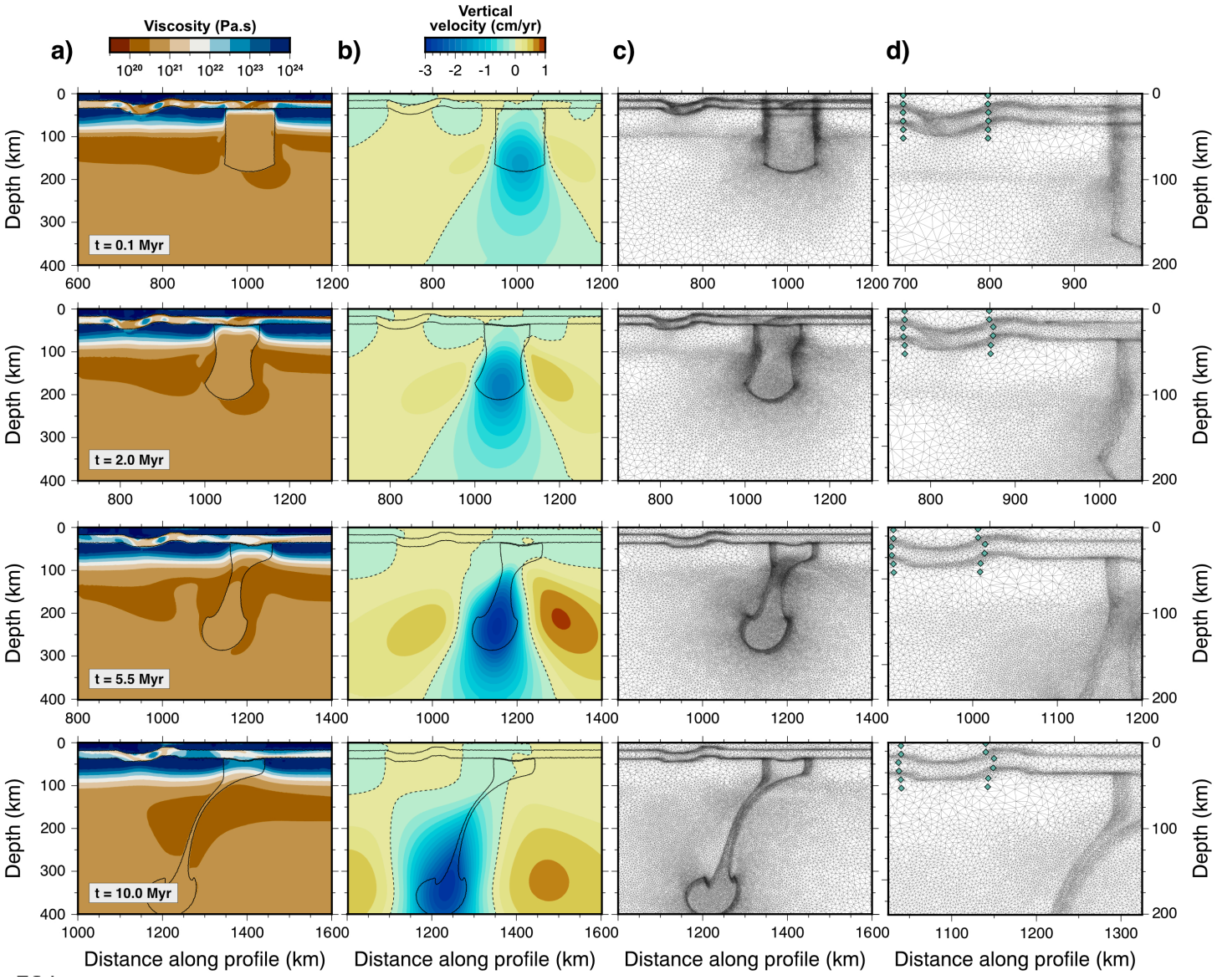

Extended Data Figure 12: Viscosity, vertical velocity and adaptive mesh. (a) viscosity at different stages of the model; (b) vertical velocity with negative and positive values indicating downwelling and upwelling, respectively. Dashed black line delineates the zero vertical velocity contour. Note that within a few Myr of drip initiation, vertical velocities become positive beneath the Crocker Range, an essential process that would facilitate melting; (c) the associated computational mesh; (d) a zoom-in of c, also illustrating particle locations. Our adaptive mesh approach achieves minimum edge-lengths of 600 meters in regions of dynamic significance (i.e., at material interfaces and in areas of high temperature and velocity gradient), with coarser resolution of up to 50 km, elsewhere. This high-resolution is essential for accurately and efficiently capturing key elements of our simulation.

Supplementary movie 1: Density and mantle flow model evolution. Upper panel shows the density field as the model evolves through 10 Myr of the simulation. The density seed is characterized by relatively higher density, illustrated in red. Bottom panel shows the mantle flow (black arrows) and vertical velocities induced by sinking of the gravitational instability through the mantle.

Supplementary movie 2: Viscosity and mesh model evolution. Upper panel shows the viscosity field as the model evolves through 10 Myr of the simulation (red is high viscosity while blue is low). Black lines are temperature contours in Kelvin at 273, 500, 750, 1000, 1250 and 1573, respectively. Bottom panel shows the underlying anisotropic dynamically-adaptive computational mesh.